

4 Three-Dimensional Probing of Catalyst Ageing on Different Length Scales: A Case Study of Changes in Microstructure and Activity for CO Oxidation of a Pt–Pd/Al₂O₃ Catalyst

Torben Nilsson Pingel,^{*[a]} Sheedeh Fouladvand,^[b] Marc Heggen,^[c] Rafal E. Dunin-Borkowski,^[c] Wolfgang Jäger,^[a] Peter Westenberger,^[d] Daniel Phifer,^[e] Jace McNeil,^[f] Magnus Skoglundh,^[b] Henrik Grönbeck,^[a] and Eva Olsson^[a]

The effects of thermal treatment on the microstructure of a Pt–Pd/Al₂O₃ oxidation catalyst and its activity for CO oxidation have been studied. The microstructural analysis was performed by using several high-resolution electron microscopy techniques such as STEM, FIB/SEM slice & view, SEM and EDX. A combination of these analytic techniques and advanced TEM specimen preparation allowed for three-dimensional probing at different length scales, avoiding the random character of conventionally crushed powder specimens owing to site specificity. A core–shell distribution of Pt–Pd nanoparticles within

the alumina support particles, with enlarged nanoparticles (≈ 1.5 to 40 nm) present in the shell and small nanoparticles (< 1.5 nm) in the core, was revealed in the untreated catalyst. A more uniform spatial distribution developed during thermal treatment at 700 °C or higher with larger nanoparticles forming in the core. Accompanying measurements of the catalytic activity for CO oxidation showed the detrimental effect of sintering of the small nanoparticles on the reaction rate and apparent activation energy of the reaction.

Introduction

Oxidation of carbon monoxide over supported Pt-based catalysts is a key reaction in environmental catalysis. It receives special attention in the context of three-way catalytic converters, diesel oxidation catalysts, and NO_x storage and reduction catalysts for vehicle exhaust abatement owing to a worldwide rising number of vehicles and increasingly stringent emission regulations.^[1]

Several studies have been performed to evaluate the activity for CO oxidation of such catalysts,^[2] microstructural and chemical changes induced by ageing treatments,^[2a,d,3] as well as the effect of alloying with other metals.^[3a,4] However, studies focusing on three-dimensional characterisation on the micro- and nanoscale of supported catalysts are scarce. A few studies used (S)TEM ((scanning) transmission electron microscopy) to-

mography^[5] and quantitative STEM,^[6] providing three-dimensional information about small volumes of the catalyst. The three-dimensional distribution of nanoparticles over micrometre-sized support structures has, however, not been properly addressed yet for this type of catalyst.

In the present work, we have studied microstructural changes of a bimetallic Pt–Pd/Al₂O₃ catalyst induced by hydrothermal ageing (500–800 °C, 24 h) and correlated these with changes in the activity for oxidation of CO. STEM was used in combination with a recently developed specimen preparation method,^[7] allowing for three-dimensional and site-specific probing of the catalyst structure on the nanoscale. These measurements were complemented by focused ion beam

[a] T. Nilsson Pingel, Prof. W. Jäger, Prof. H. Grönbeck, Prof. E. Olsson
Competence Centre for Catalysis, Department of Physics
Chalmers University of Technology
41296 Gothenburg (Sweden)
E-mail: torben.nilsson.pingel@chalmers.se

[b] Dr. S. Fouladvand, Prof. M. Skoglundh
Competence Centre for Catalysis,
Department of Chemistry and Chemical Engineering
Chalmers University of Technology
41296 Gothenburg (Sweden)

[c] Dr. M. Heggen, Prof. R. E. Dunin-Borkowski
Ernst Ruska-Centre for Microscopy and Spectroscopy with Electrons
and Peter Grünberg Institute
Jülich Research Centre
52425 Jülich (Germany)

[d] P. Westenberger
FEI—Visualization Sciences Group
40237 Düsseldorf (Germany)

[e] D. Phifer
FEI—Science Group
5651 GG, Eindhoven (The Netherlands)

[f] J. McNeil
FEI—Hillsboro
97124 OR (USA)

Supporting information and the ORCID identification number(s) for the author(s) of this article can be found under <https://doi.org/10.1002/cctc.201700479>.

This publication is part of a Special Issue on “Advanced Microscopy and Spectroscopy for Catalysis”.

(FIB)/SEM slice & view tomography which gives three-dimensional information for larger volumes on the microscale.

Thus, it became possible to reveal an inhomogeneous spatial distribution of catalyst nanoparticles within the support as well as the sintering of nanoparticles (meaning nanoparticle growth by particle migration and coalescence and/or Ostwald ripening). The degree of sintering at different temperatures varied with nanoparticle size. An increase of Pt–Pd intermixing in the catalytic nanoparticles after ageing could be observed by STEM using energy-dispersive X-ray spectroscopy (EDX). Activity measurements of CO oxidation showed a clear decrease in catalytic activity after heat treatment, which could be correlated with sintering of small Pt–Pd nanoparticles and clusters observed by STEM. Also, the apparent activation energy of the reaction increased after the heat treatments.

This study gives new insight into the three-dimensional distribution of the active material within supported nanoparticle catalysts. Moreover, the new approaches regarding TEM specimen preparation and three-dimensional characterisation can be used in other fields of catalysis research to obtain valuable additional spatially resolved structural information of heterogeneous catalysts.

Results and Discussion

Effect of ageing on the microstructure—nanoparticle sintering and spatial distribution

To determine the microstructural changes of the Pt–Pd/Al₂O₃ catalyst induced by the thermal treatment, several electron microscopy techniques were employed. The thermal treatment was performed *ex situ* before specimen preparation in all parts of this study. High-resolution STEM was used to investigate and follow the spatial distribution and sizes of the catalytic Pt–Pd nanoparticles. The TEM specimens were prepared by a FIB/SEM specimen preparation method described recently^[7] that enabled the observation of individual oxide support particles in a cross-section view and revealed an inhomogeneous spatial distribution of nanoparticles. We observed extensive sintering of small nanoparticles as a result of thermal ageing at 700 °C and higher.

STEM images of the interior of the alumina support (Figure 1 left column) and the outer edge of the support (Figure 1 right column) were analysed before and after heat treatment. The observed nanoparticles were divided into three groups to simplify the discussion:

- Small nanoparticles: diameters of 1.5 nm and below (some marked by red circles)
- Medium-sized nanoparticles: diameters from 1.5 nm to 10 nm (some marked by green circles)
- Large nanoparticles: above 10 nm in diameter (some marked by blue circles)

The near-edge regions of the samples before ageing (Figure 1a right) contained all three size groups of catalyst nanoparticles. Whereas the small nanoparticles could be observed

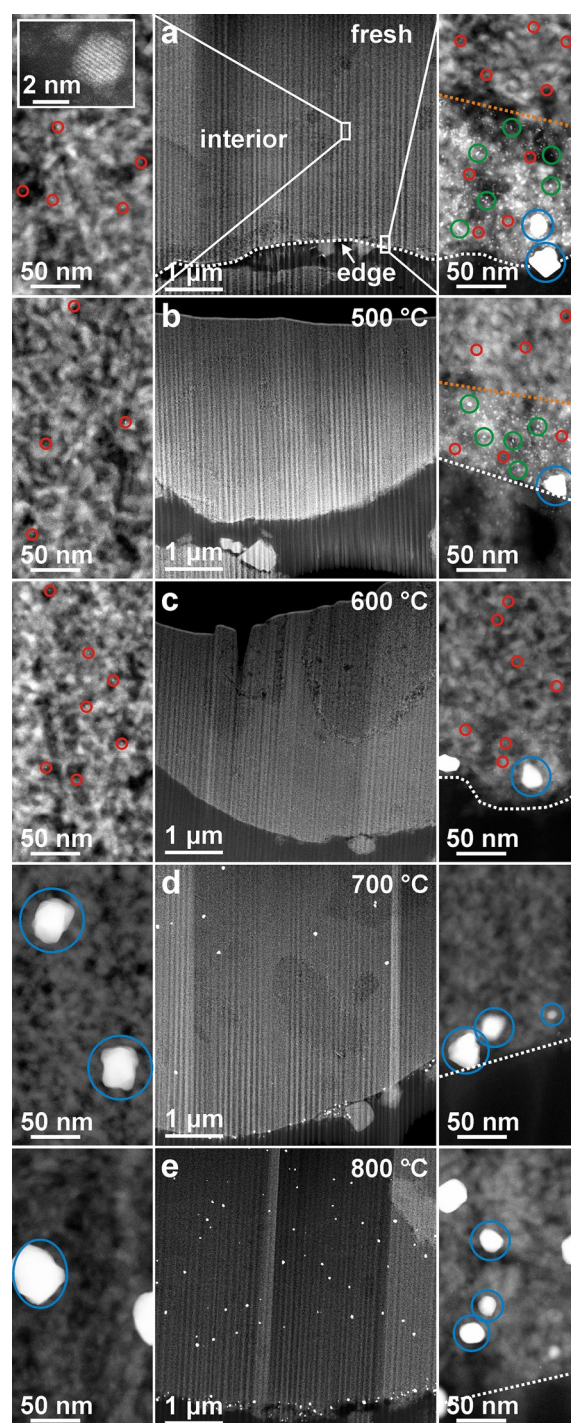


Figure 1. HAADF STEM images of a) fresh and b–d) aged catalyst samples prepared by the FIB/SEM lift-out method. Central column: low-magnification overview images of each specimen, left column: images at higher magnification from regions in the interior of the alumina support, right column: regions at the outer edge. Pt–Pd nanoparticles show bright contrast. Inset in (a): medium-sized nanoparticle at high resolution. At higher magnification, the porous alumina structure can be seen in the background. The edge of the alumina support is marked by a white dotted line. Some Pt–Pd nanoparticles are highlighted by circles (red: small NPs, green: medium-sized NPs, blue: large NPs). The orange dotted line marks the inner boundary of a layer with an increased density of medium-sized nanoparticles.

over the entire region, the medium-sized nanoparticles were confined to an outer layer of approximately 100–200 nm thickness (the inner boundary of that layer is indicated by an orange dotted line). The large nanoparticles were confined to the very outer edge of the support, as the low-magnification overview image (Figure 1a centre) showed no indication of large nanoparticles anywhere in the interior.

Small nanoparticles are hardly visible at these magnifications. However, they are easily detectable at higher magnifications. As an illustration, the inset in Figure 1a shows a STEM image of a Pt–Pd catalyst nanoparticle with a diameter of approximately 2.5 nm at atomic lattice resolution. A STEM image at high magnification is shown in Figure 2, illustrating the presence of irregularly shaped clusters as well as single Pt and/or Pd atoms on the alumina support in addition to small crystalline nanoparticles.

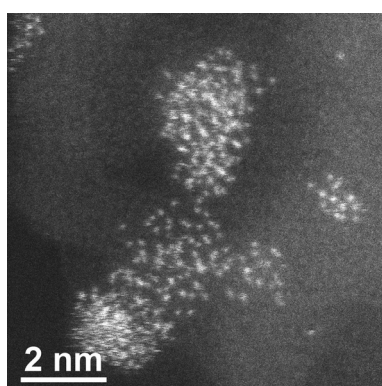


Figure 2. HAADF STEM image of irregularly shaped Pt–Pd clusters and single atoms in the untreated catalyst sample. These could be observed in addition to small crystalline nanoparticles (Figure 1a). The contrast seen in these clusters suggests a flat, raft-like shape on the alumina surface.

The image of the interior of the sample before ageing (Figure 1a left) shows the presence of almost exclusively small nanoparticles with a high density in that region; only a few of these catalyst nanoparticles are highlighted. The inhomogeneity regarding nanoparticle sizes, with exclusively small nanoparticles in the interior of the alumina support and medium-sized as well as a few large nanoparticles close to the outer edge, originates very likely from precipitation of larger amounts of the Pt–Pd precursor at the outer edge of the alumina in the drying step of the wet impregnation.^[8] During the successive calcination, this higher precursor concentration led to the formation of enlarged nanoparticles at the outer edge.

After ageing at 500 °C, the catalyst support with the Pt–Pd catalyst nanoparticles appeared largely unchanged (Figure 1b), the catalyst nanoparticles in the interior of the support particle were small and an outer layer with a high density of medium-sized nanoparticles was visible, as well as a few large nanoparticles at the outer support particle edge.

A detailed quantitative nanoparticle size analysis (Figure 3) revealed only a slight change in nanoparticle sizes close to the outer support particle edge as compared to the sample before

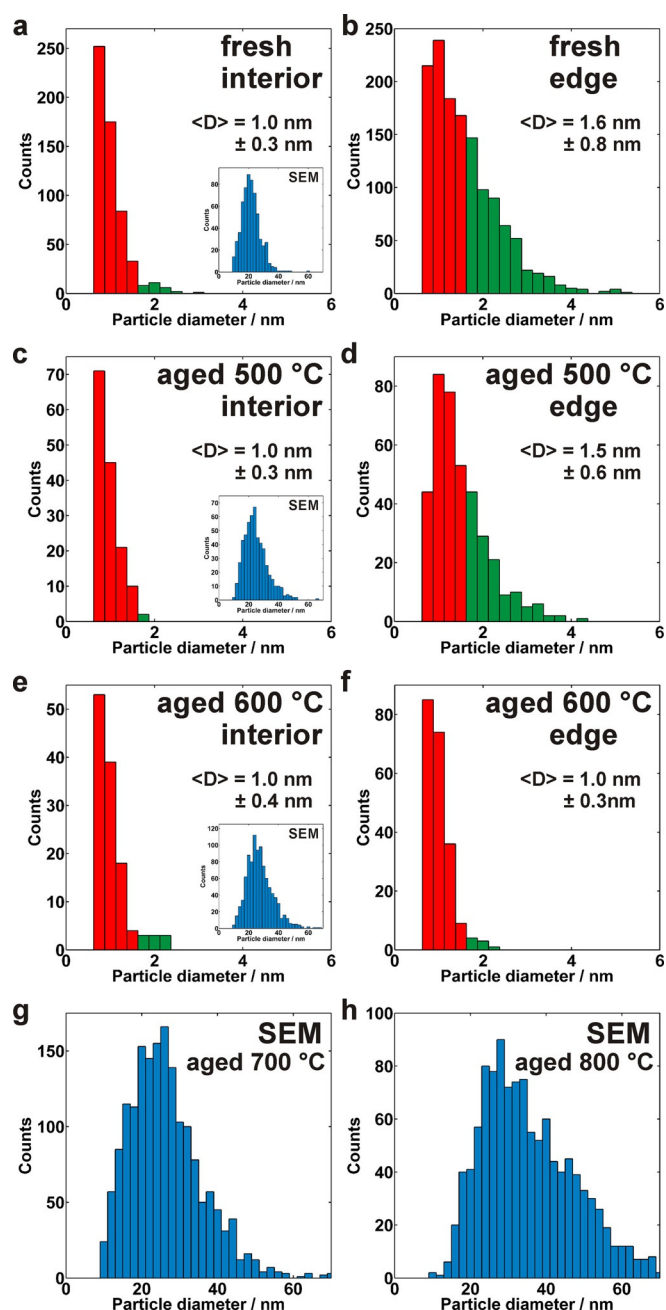


Figure 3. a–f) Particle-size distributions (PSDs) of Pd–Pt nanoparticles for the fresh and 500 and 600 °C aged specimens as obtained from STEM images. Left: PSDs obtained from interior regions, right: PSDs from regions at the outer edge of the alumina support. The same colour coding for particle size as in Figure 1 is used. Nanoparticles above 6 nm were not included because of their low number in the STEM images. The insets show PSDs of the large NPs obtained by SEM. g, h) PSDs of the large nanoparticles obtained by SEM after ageing at 700 and 800 °C. PSDs of the small and medium-sized NPs are not shown because these vanished almost completely after the heat treatment.

ageing. The average nanoparticle size in the interior was 1.0 nm before and after ageing at 500 °C, and 1.6/1.5 nm, respectively in the outer layer of the support. For this analysis, only nanoparticles with diameters above 0.6 nm were considered to ensure reliable particle detection.

Ageing at 600 °C led to noticeable sintering of the metal nanoparticles in the catalyst, which, interestingly, mainly influenced the medium-sized nanoparticles (Figure 1 c). The region close to the outer edge still contained small and large catalyst nanoparticles, whereas the medium-sized ones had vanished and likely sintered forming a small number of additional large nanoparticles. This can be seen in Figure 3 e,f; the edge and interior of the catalyst support particles have basically the same nanoparticle sizes (average: 1.0 nm) after ageing at 600 °C with the exception of a few large nanoparticles near the edge (not seen at this scaling). The size distribution of the large nanoparticles (diameter of 10 nm or larger) was investigated by SEM for all ageing temperatures and is depicted as insets in Figure 3, as well as in more detail in the Supporting Information (Figure S1).

Possible factors explaining the pronounced sintering of the medium-sized nanoparticles are the proximity of these in the fresh sample, as well as a stabilisation of the small nanoparticles because a higher fraction of metal atoms is in direct contact with the alumina support. This results in sintering and the disappearance of most catalyst nanoparticles in the range of 1.5 to 4 nm, whereas many nanoparticles below 1.5 nm remain.

After ageing at 700 °C, sintering of the small nanoparticles could be observed (Figure 1 d). Large Pt–Pd nanoparticles were located in the interior of the alumina support, which is visible both in the overview image and the close-up on the left side. Although a few small nanoparticles remained in some areas, their number was strongly reduced. As the small nanoparticles were homogeneously distributed within the alumina support before heat treatment and the large nanoparticles appear evenly distributed after heat treatment as will be shown below (except the outer alumina edge, which contains a higher noble-metal content before and after ageing), our study suggests a quite local sintering, without major net transport of Pt and Pd across the alumina support. The exact sintering mechanism though, for example if atomic or crystalline migration dominates, cannot be deduced by these post-mortem experiments using realistic catalyst samples.

Ageing at 800 °C resulted in even stronger sintering, removing basically all small nanoparticles and forming slightly larger nanoparticles as compared to ageing at 700 °C.

Three-dimensional nanoparticle distribution

To confirm and quantify the spatial distribution of large nanoparticles, FIB/SEM slice & view tomography of the untreated and 800 °C aged sample was performed. Catalyst nanoparticles with diameters above 10 nm could be investigated using this technique. We could detect that most of the large nanoparticles were situated within 100 nm of the outer support edge in the untreated sample, whereas the spatial distribution was largely uniform after high-temperature ageing at 700 °C or higher.

The spatial distribution of the large nanoparticles was already indicated by the STEM investigation. STEM images showed that the large catalyst nanoparticles were only present

at the outer edge of the catalyst support particles for the untreated sample, whereas they appeared in the interior after ageing at 700 and 800 °C. Using the slice & view technique, a micrometre-sized three-dimensional volume could be investigated. The spatial distribution of large nanoparticles was quantified for a much larger number of nanoparticles than by the STEM investigation.

Illustrations of the three-dimensional datasets for the fresh (Figure 4 a) and aged (Figure 4 b) sample clearly show differences in the spatial distribution of nanoparticles within the support particles. The distribution of distances between the catalyst nanoparticles and the support particle edge shows that most of the large nanoparticles were situated within 100 nm to the outer edge of the alumina support in the fresh sample (Figure 4 c). The measured distances correspond to the real three-dimensional distances and are not obtained from projected images but from reconstructed three-dimensional volumes. The average of the distances from the catalyst nanoparticles to the edge of the alumina support in the investigated alumina particle was 36 nm.

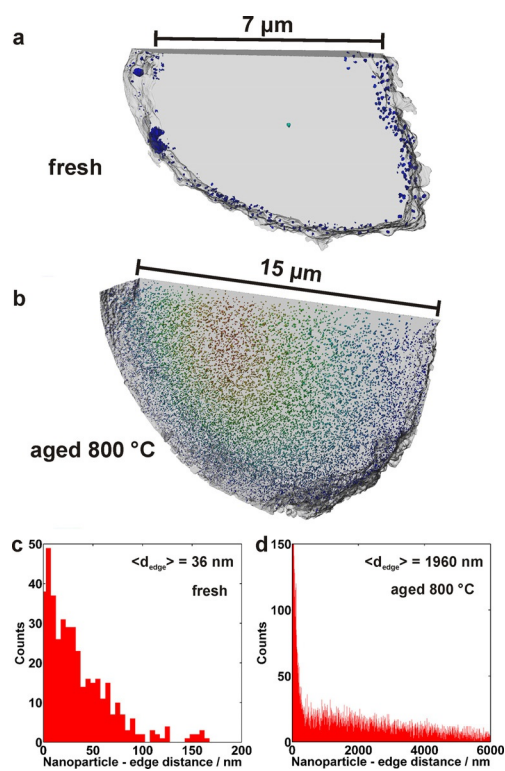


Figure 4. Results of FIB/SEM slice & view tomography of the fresh and the 800 °C aged sample. a) Slice of a three-dimensional reconstruction showing Pt–Pd nanoparticles distributed within an alumina support particle with a diameter of approximately 7 µm. Nanoparticles larger than 10 nm could be observed using this technique. The nanoparticles were mainly distributed along the outer edge of the alumina support, only very few ones could be found inside the support. b) Respective illustration of an alumina particle after ageing at 800 °C. The Pt–Pd nanoparticles were evenly distributed within the alumina support except a high concentration very close to the outer edge. The NPs are colour-coded by their distance to the alumina edge. c, d) Distribution of distances from the nanoparticles to the edge of the alumina support for the fresh and aged sample.

After ageing at 800 °C (Figure 4d), large catalyst nanoparticles could be seen in the interior of the alumina support particle. There clearly still was a high concentration of large catalyst nanoparticles close to the support edge, but additional nanoparticles could be seen several micrometres away from the support edge in the interior of the support particle. Inside of the (approximately spherical) alumina support particle, the number of Pt–Pd nanoparticles was roughly inversely proportional to their distance to the support edge (graph in Figure 4d decays roughly linearly except in the near-edge region). This indicates an even density of large nanoparticles within the support, meaning the sintering occurred homogeneously over most of the alumina support. This also supports our suggestion about local sintering of the noble metals. In the near-edge region the number and sizes of Pt–Pd nanoparticles before sintering were higher compared to the interior as was shown by STEM imaging (Figure 1a), resulting in more large nanoparticles after heat treatment as can be seen in Figure 4d. A quantification of the nanoparticle nearest neighbour distances can be found in the Supporting Information, Figure S2.

The possibility of an investigation of the three-dimensional spatial nanoparticle distribution inside of a catalyst support material over such a large volume is today unique to the FIB/SEM slice & view technique. In the present work, this technique allowed a confirmation of the spatial nanoparticle distribution observed in the TEM, as well as a quantification of a much larger sample volume compared to TEM, resulting in considerably better statistics.

Chemical composition and Pt–Pd intermixing

Chemical characterisation of individual nanoparticles was performed for the fresh and aged samples (600, 700 and 800 °C) to investigate their chemical composition and compositional changes induced by the ageing. Energy-dispersive X-ray spectroscopic (EDX) analysis was mainly performed in STEM mode in the TEM, and some control measurements of large nanoparticles in thin TEM specimens were conducted using EDX analysis in SEM, which showed results consistent with the STEM experiments.

A consistent result of the analysis of the fresh sample was an enrichment of platinum in the large nanoparticles (> 10 nm) compared to the nominal composition of 85 wt.% Pt/15 wt.% Pd. The composition of the nanoparticles varied with particle size, larger particles had higher Pt and lower Pd contents. For example, nanoparticles with diameters above 30 nanometres consistently showed Pd contents of 5 wt.% or less, particles between 20 and 30 nm contained up to 10 wt.% Pd with a few exceptions, while some smaller particles around and below 10 nanometres showed Pd enrichment with up to about 30 wt.%.

The variation of the Pd content in small nanoparticles was, however, quite large. Nanoparticles below 10 nm had a Pd content between 5 and 30 wt.%. Overall, these results show that small nanoparticles and regions containing clusters and single atoms were slightly enriched in Pd, in accordance with

studies by Johns et al.^[4a] and Ezekoye et al.^[4d] on bimetallic Pt–Pd catalysts.

After ageing at 600 °C, no significant differences could be observed. After ageing at 700 and 800 °C, the Pd concentration in the large nanoparticles was considerably higher. Nanoparticles in the size range of 10 to 70 nm had Pd concentrations of 15 to 30 wt.%. This is also in accordance with the study by Ezekoye et al., who found a higher degree of Pt/Pd intermixing after thermal ageing.^[4d] Some large particles with diameters above 100 nm and a lower Pd content of about 10 wt.% were observed, consistent with the trend that the largest particles appear to be rich in platinum. Platinum is also known to form so-called anomalously large nanoparticles during high-temperature ageing in an oxygen-rich atmosphere, mainly through vapour-phase transport.^[4c,d] These anomalously large nanoparticles, though relatively few, contain large amounts of Pt and could explain the slightly higher Pd concentration in the “normal” large nanoparticles.

It is important to notice that most large nanoparticles observed after the heat treatment resulted from sintering of the previously observed small nanoparticles, whereas the large nanoparticles in the fresh sample are a result of the catalyst preparation and were formed simultaneously with the small nanoparticles. What was observed here is therefore not a change in chemical composition of the large nanoparticles, but the formation of a new population of large, slightly Pd-enriched nanoparticles by sintering of the small ones.

Previous studies have shown that Pt is very mobile at high temperatures in oxidising environments and can be effectively trapped by PdO nanoparticles.^[4f,g] The studies demonstrated that upon heat treatment of specimens with initially separated Pt and PdO nanoparticles, the highly mobile Pt is trapped by the more stable PdO nanoparticles and alloyed Pt–Pd nanoparticles are formed, which are thermodynamically more stable and slow down further sintering by Ostwald ripening as well as the emission of Pt into the vapour phase.^[4h] It has also been shown that bulk PdO basically does not sinter at temperatures below the oxide decomposition temperature which lies above 800 °C, because sintering mainly occurs in the metallic form.^[3c]

In our study, we clearly see sintering of the Pd species, as Pd is finely dispersed in the fresh sample and concentrated in a small number of large nanoparticles after high-temperature treatment. If the Pd was fixed on the surface and only Pt would sinter and be trapped by PdO nanoparticles, there should be a larger number of smaller nanoparticles after ageing (larger nanoparticles than in the fresh sample, but much smaller than what we observe). The reason behind the sintering of Pd is that it is not present in the form of PdO, but alloyed with Pt, which keeps it in a metallic state.^[4a,h] In this way, Pt increases the rate of the Pd sintering. The observations about the sintering of Pt and Pd made in the present study are, therefore, in agreement with these relatively recent studies.

STEM EDX mapping was performed to investigate the intermixing of Pt and Pd within some larger nanoparticles in the fresh and 800 °C aged sample. In the fresh sample, a core–shell structure with a Pd rich shell could be seen for some of the in-

vestigated nanoparticles (Figure 5). The Pd map in the upper right corner shows image pixel intensities corresponding to the local Pd concentration in the sample and indicates a clear enrichment of Pd around the rim of the nanoparticle. In the sample aged at 800 °C, in which the overall Pd content of the large nanoparticles is much higher, no core-shell structures were found. The observed nanoparticles appeared to be homogeneously alloyed (Figure 5, lower part). Sum spectra of these nanoparticles, showing the higher Pd content after ageing, can be found in the Supporting Information (Figure S3).

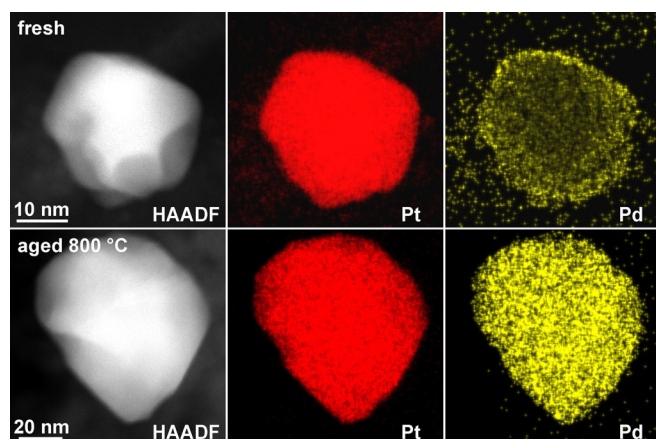


Figure 5. HAADF STEM images and STEM EDX elemental maps of Pt–Pd nanoparticles in the fresh and 800 °C aged specimen. The pixel intensities in the elemental maps represent the concentrations of the elements measured at that position.

Whereas the total Pt/Pd concentrations of the large nanoparticles could be observed over a wide range of nanoparticles both in STEM as well as in SEM and are therefore representative, the detailed elemental maps in Figure 5 showing the elemental distribution within individual nanoparticles were experimentally much more challenging to obtain and were only obtained for a few nanoparticles in the fresh and aged samples. We can, therefore, not quantify how many nanoparticles in the fresh sample exhibit a core-shell structure, but we can demonstrate that these structures exist and that there tends to be a difference in structure before and after the heat treatment.

In summary, the EDX measurements showed an enrichment of Pd in the small nanoparticles and clusters of the fresh catalyst and increasing Pt–Pd intermixing after high-temperature ageing and sintering. In the fresh catalyst, some of the large nanoparticles exhibited a core-shell structure with a Pd-rich shell, which was not observed after ageing at 800 °C.

Catalytic activity for CO oxidation

CO conversion at low temperatures (≤ 100 °C) was measured using a continuous-flow reactor to link the observed microstructural changes to the catalytic activity of the catalyst. We found a clear correlation between the activity for CO oxidation and sintering of small nanoparticles and clusters in the sample.

The CO conversion decreased steadily if increasing the ageing temperature. The conversion of CO at 100 °C decreased from 37 to 7% after ageing at 800 °C (Figure 6). A clear decrease of catalytic activity in the entire measured temperature range was observed already after ageing at 500 °C. The STEM analysis

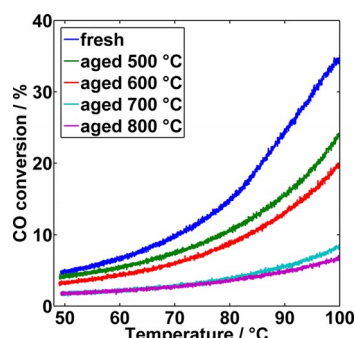


Figure 6. Activity for CO oxidation of the fresh and aged catalyst samples. The conversion measurements were performed in a continuous-flow reactor during a cooling ramp in 4% O₂ and 1000 ppm CO balanced with argon.

performed with specimens aged at this temperature indicated no major difference in the observed nanoparticle sizes (Figure 3a–d). Sintering might, however, have occurred for very small nanoparticles ($d < 0.6$ nm), clusters and single atoms. These were not always reliably detectable in all regions of the sample and therefore not quantifiable. The nanoparticles above the detection limit of about 0.6 nm, on the other hand, did evidently not change under these mild ageing conditions (Figure 3a–d), whereas the catalytic activity clearly did (Figure 6). This is an indirect indication by the combined STEM observations and flow reactor results that sintering of very small Pt–Pd structures below 0.6 nm in diameter has a significant influence on the catalytic activity for CO oxidation. This conclusion is in agreement with other studies that have also suggested the importance of small clusters and single atoms for the low-temperature catalytic activity.^[9]

After ageing at 600 °C, the catalytic activity decreased only slightly compared to ageing at 500 °C. This probably owes to the low number of the medium-sized nanoparticles which sintered at this temperature compared to the number of the remaining small nanoparticles. The measured sizes of the small nanoparticles did not change noticeably (Figure 3c,e), but as mentioned above, there might have been changes to nanoparticles and clusters below 0.6 nm having an effect on the catalytic activity. The activity strongly decreased after ageing at 700 °C. As the STEM imaging revealed the onset of strong sintering of small nanoparticles at this temperature (Figure 1d), the correlation with the activity demonstrates the importance of highly dispersed catalytic species for this reaction. After ageing at 800 °C, there was only a slight further reduction of activity compared to the sample aged at 700 °C. This is not surprising, since the microstructures of these samples were similar with respect to the very low fractions of small nanoparticles.

The apparent activation energies for CO oxidation were determined from the activity measurements. The rate constant k

of the catalysed chemical reaction between CO and O₂ exhibits an exponential behaviour as a function of the reaction temperature T (Equation 1):

$$k \propto e^{-\frac{E_a}{RT}} \quad (1)$$

where E_a is the apparent activation energy and R the ideal gas constant. The conversion follows this exponential behaviour as long as the reaction rate is low and therefore limited by the chemical kinetics rather than mass transport of reactants to the active sites.^[1a,10] The apparent activation energies E_a of the different samples can then be determined by applying fits to the CO conversion profiles. To ensure that mass-transport limitations are not influencing our results, only data from temperature intervals corresponding to low conversions, between 5 and 15%, was used for this analysis. Potential mass-transport limitations were ruled out using the Weisz–Prater criterion^[11] as shown in the Supporting Information.

The apparent activation energies determined in our experiments are summarised in Table 1 and lie within the range of values normally reported for CO oxidation over Pt-based catalysts. This reported range is quite broad and the obtained values depend strongly on the material and experimental con-

Table 1. Apparent activation energies for CO oxidation determined from continuous flow reactor experiments. The apparent activation energy increased after heat treatment at high temperatures.

Ageing temperature [°C]	E_a [kJ mol ⁻¹]
Fresh	36
500	34
600	39
700	48
800	45

ditions. Nicholas and Shah reported an activation energy for CO oxidation of 27 kJ mol⁻¹ over a Pt catalyst supported on porous fibre glass,^[12] whereas Akubuiro et al. reported a value of 92 kJ mol⁻¹ over a Pt/Al₂O₃ catalyst.^[13] Other reported values are 112 kJ mol⁻¹,^[14] 54–92 kJ mol⁻¹,^[2b] and 62 kJ mol⁻¹.^[2a] The apparent activation energies for CO oxidation determined in the present investigation increased from 36 kJ mol⁻¹ to 48 kJ mol⁻¹ after ageing at 700 °C. Other studies have contrarily reported a decrease in apparent activation energy for CO oxidation with decreasing dispersion of Pt-based catalysts.^[2a,b,e] These studies, however, partly used different experimental conditions as well as different support materials such as silica.

The Pt–Pd/Al₂O₃ catalyst investigated in the present study appears to exhibit an increase in apparent activation energy for CO oxidation at low temperatures as the nanoparticle sizes and the degree of Pt–Pd intermixing increase with ageing. Our results are in accordance with a study of Chen et al., who investigated Pt-based catalysts with different dispersions owing to different metal loadings or support materials.^[2c] They determined a higher catalytic activity for CO oxidation near room temperature for higher dispersions. In the present work, the

same behaviour is demonstrated using only one catalyst and ageing at different temperatures.

Our results clearly show the predominance of small nanoparticles for CO oxidation over this Pt–Pd/Al₂O₃ catalyst. One clear indication is the drop of activity for CO oxidation already after ageing at 500 °C, at which temperature no evident changes in the size distribution of particles around one nanometre in diameter were observed. Sintering of Pt–Pd nanoparticles and clusters below 0.6 nm in diameter is the most likely explanation for this behaviour. The second indication for the importance of small nanoparticles is the considerable decrease in activity after ageing at 700 °C (Figure 6), the temperature for which the STEM results revealed strong sintering of small nanoparticles and typical diameters of above 10 nm for the resulting nanoparticles (Figure 1d). The importance of the small nanoparticles for the activity is also supported by the determined apparent activation energies for CO oxidation that show a significant increase after ageing at 700 °C.

Total internal surface area

To investigate the influence of the ageing procedures on the alumina support structure, total internal surface area measurements according to the BET method were conducted (Table 2).

Table 2. Total surface area of the fresh and aged catalyst samples determined by physisorption of nitrogen at –196 °C (BET method).

Ageing temperature [°C]	BET surface area [m ² g ⁻¹]
Fresh	175
500	162
600	168
700	138
800	122

As expected, the internal surface area became lower after ageing at high temperatures, especially at 700 and 800 °C, owing to the coarsening of the support structure. This effect, however, does not account for the considerable decrease of catalytic activity that was observed by the CO oxidation experiments. Hence, the microstructural changes of the Pt–Pd nanoparticles described above are most likely the main factor for the observed decrease in activity for CO oxidation.

Conclusions

In the present work, we demonstrated the importance of small Pt–Pd nanoparticles and clusters for the oxidation of CO over a bimetallic Pt–Pd/Al₂O₃ catalyst. To analyse the microstructure of the fresh and aged catalyst samples, a combination of different site-specific electron microscopy techniques and advanced TEM specimen preparation were used that revealed the three-dimensional structure of the catalyst and distribution of Pt–Pd nanoparticles from the nano- to the microscale. This analysis was accompanied by measurements of the activity for CO oxidation.

Before heat treatment, most detectable nanoparticles were in the size range of 0.6 to 1.5 nm. Already a mild heat treatment at 500 °C reduced the activity noticeably which suggested sintering of small catalytic nanoparticles below 0.6 nm in diameter. Nanoparticles in this size range appear to have a considerable influence on the total activity of the catalyst. Heat treatment at temperatures of 700 °C and higher resulted in sintering of almost all nanoparticles below 10 nm in diameter. Consequently, the activity for CO oxidation considerably decreased and the apparent activation energy for the reaction increased. This is strong evidence for a particle-size dependence of the activity for CO oxidation with a predominance of catalytic nanoparticles below 1.5 nm in diameter. In addition to the higher total surface area that small nanoparticles provide, our measurements also show an inherent higher activity for CO oxidation of smaller nanoparticles in this catalyst, which is deducted from the higher apparent activation energy after heat treatment and sintering. The observed sintering of the Pd species in this catalyst demonstrates the destabilisation of Pd caused by alloying with Pt in comparison to a pure Pd catalyst under oxidising conditions, as was described in other recent studies.

Attention was paid to the distribution of Pt and Pd within the larger catalyst nanoparticles. The local concentrations of Pt and Pd in nanoparticles were determined by energy-dispersive X-ray spectroscopy (EDX) mapping. A core-shell structure was observed in some large nanoparticles in the untreated sample, containing a higher concentration of Pd in the shell. After heat treatment at 800 °C, uniform distributions of Pt and Pd were observed.

To reach these conclusions, we successfully used new approaches for the TEM specimen preparation providing access to the three-dimensional structure of the catalyst samples on different length scales. Our approach can be applied to many other systems of supported catalysts and might reveal new microstructural properties that were so far overlooked in routine investigations.

Experimental Section

Catalyst sample

In this work, a commercially produced emission-control catalyst has been investigated. The catalytically active phase consists of Pt-Pd catalyst nanoparticles supported on a porous γ -alumina substrate. The noble-metal loading is 0.17 wt.% platinum and 0.03 wt.% palladium (Pt/Pd atomic ratio of 3.1:1). The diameter of the alumina support particles, consisting of agglomerates of γ -alumina primary particles, is typically in the range of several micrometres.

Hydrothermal ageing

The catalyst samples were hydrothermally aged in a controlled atmosphere at four different temperatures: 500, 600, 700 and 800 °C using a continuous-flow reactor. The temperature was measured by a thermocouple inserted into the catalyst bed and the atmosphere was regulated using mass flow controllers. All samples were flushed in pure argon for several minutes at room temperature

before the ageing experiments and then heated to their respective ageing temperature at a heating rate of 7 °C min⁻¹. After reaching the final temperature, the samples were exposed to an atmosphere of 75 vol.% argon, 15 vol.% oxygen and 10 vol.% water for 24 h. Oxygen and water vapour are constituents of real engine exhausts and have repeatedly been shown to promote nanoparticle sintering.^[15] Following this treatment, the samples were cooled in pure argon for approximately two hours before removing them from the reactor.

Transmission electron microscopy

Transmission electron microscopy imaging was conducted using an FEI (Hillsboro, Oregon, USA) Titan 80–300 TEM/STEM instrument operated at an acceleration voltage of 300 kV. The instrument is equipped with a field-emission electron source and a probe aberration corrector, enabling a spot diameter of the focused probe below 0.1 nm in STEM mode. To detect small nanoparticles on the corrugated support structure, the probe was scanned over the specimen and parts of the scattered electrons were collected using a high-angle annular dark-field (HAADF) detector. As the probability of electron scattering to high angles strongly increases with the atomic number *Z* of the atoms interacting with the electron beam, so-called Z-contrast images can be obtained that provide a strong bright image contrast even for very small Pt–Pd nanoparticles.

Chemical characterisation was performed by using energy-dispersive X-ray spectroscopy (EDX) in an FEI Titan 80–200 TEM/STEM instrument equipped with a Super-X EDX detector and a probe aberration corrector, as well as an FEI Titan 80–300. Before quantification, background subtraction in the EDX spectra was performed. Pt-L and Pd-L peaks were analysed to obtain their relative concentrations. To minimise contaminations by carbon species, the specimens were cleaned in diluted oxygen plasma before inserting them into the microscope.

TEM specimen preparation methods

Traditional crushing method. Catalyst specimens prepared by this method were crushed in a mortar, dispersed in analytical grade alcohol and subsequently deposited onto a holey carbon film supported by a copper grid.

Lift-out method. Specimen lift-out of lamellae catalyst support particles and transfer into the microscope has been applied in these experiments. The specimen lamellae were prepared using an FEI Versa 3D DualBeam focused ion beam/ scanning electron microscope (FIB/SEM). After embedding the catalyst powder in acrylic resin (LR white, hard grade), slices from individual catalyst oxide support particles were cut by a gallium ion beam and extracted using a micromanipulator following a procedure described earlier.^[7] The resulting specimen lamellae showed the catalyst support particles together with the distributions of metallic catalyst nanoparticles in a cross-section view, allowing the comparison of interior parts to regions close to the outer support particle edge.

Scanning electron microscopy

Scanning electron microscopy (SEM) applying backscattered electron (BSE) contrast imaging of the catalyst samples was performed using a Zeiss (Oberkochen, Germany) Ultra-55 SEM instrument operated at an acceleration voltage of 10 kV. Before the SEM investigation, the catalyst powder was embedded in acrylic resin and me-

chanically polished, creating a cross-section view of a majority of the catalyst support particles that are exposed at the polished surface. Subsequently, a thin layer of carbon was evaporated onto the specimen surface to increase the electrical conductivity and avoid charging. A backscattered electron detector was used, the image contrast was, therefore, mainly determined by differences in the local chemical composition of the sample, thus resulting in clear visibility of the Pt–Pd nanoparticles within the alumina support. For chemical characterisation using EDX in the SEM, thin TEM specimens were used to improve spatial resolution.

Particle-size analysis

For both the SEM and TEM studies, particle-size distributions of the Pt–Pd nanoparticles were obtained from images showing the particle projected areas. Multiple images of different regions at a constant magnification were acquired and the projected areas of the catalyst nanoparticles were measured using the software ImageJ.^[16] From these areas, the projected area diameters of the nanoparticles (equivalent diameter of a spherical particle with the same projected area), the average diameter (arithmetic mean) and the standard deviation were calculated.

Total internal surface area measurement

The total internal surface area of the porous catalyst samples was determined by nitrogen adsorption at -196°C using a Micromeritics (Norcross, Georgia, USA) Tristar instrument, followed by evaluation using the (BET) method.^[17] The samples were degassed in vacuum before the experiment.

Catalytic activity measurements for CO oxidation

The catalytic activity for CO oxidation was measured in a continuous-flow reactor consisting of a quartz tube surrounded by a metal coil for resistive heating and insulated with quartz wool. The catalyst temperature was measured by a thermocouple inserted into a channel in the centre of the washcoated ceramic monolith (details below). The inlet gas concentrations (vol.%) were controlled by mass flow controllers, the outlet gas composition was analysed using a quadrupole mass spectrometer (Pfeiffer Vacuum (Asslar, Germany) Prisma).

CO oxidation experiments were performed using the following protocol: The washcoat material (200 mg, weight after drying) was coated onto a ceramic cordierite monolith (Corning Inc. (Corning Inc., New York, USA), 400 cps, $L = 15\text{ mm}$, $\varnothing = 12\text{ mm}$) from a washcoat slurry containing 80% water, 16% powder catalyst and 4% boehmite. After insertion into the reactor tube, the samples were heated in pure argon (total gas flow of 500 mL min^{-1} , corresponding to a space velocity of 17650 h^{-1}) to 450°C using a heating rate of $5^{\circ}\text{C min}^{-1}$. 4 vol.% oxygen was added to the gas flow for 10 min to obtain a similar oxidation state for all samples prior to the experiment. After that, a gas mixture containing 4% O_2 and 1000 ppm CO, balanced with argon, was introduced into the reactor and the outlet gas composition was analysed using the mass spectrometer to measure the conversion of CO to CO_2 . The catalysts were then cooled to 50°C and heated to 450°C two times to ensure reproducibility of the experiment.

FIB/SEM slice & view tomography

Three-dimensional analysis of the catalyst samples was performed by slice & view tomography using an FEI Helios NanoLab FIB/SEM. The embedded and polished catalyst samples were imaged using an electron beam and a backscattered electron detector, such as in conventional SEM imaging. After each image, a gallium ion beam was used to remove a thin slice of a few nanometres thickness from the surface, after which a new SEM image was acquired. In this way, a stack of images was recorded while cutting several micrometres into the material. Using FEI Avizo 3D reconstruction and analysis software, a three-dimensional model of the distribution of Pt–Pd catalyst nanoparticles in the alumina support could be created from the images, containing information about the actual three-dimensional locations of the nanoparticles within the alumina support volume, in contrast to the two-dimensional projected images obtained from conventional SEM or TEM imaging. All measured distances correspond to the real three-dimensional distances as obtained from the three-dimensional reconstruction.

Acknowledgements

This work has been performed within the Competence Centre for Catalysis, which is hosted by Chalmers University of Technology and financially supported by the Swedish Energy Agency and the member companies AB Volvo, ECAPS AB, Haldor Topsøe A/S, Scania CV AB, Volvo Car Corporation AB and Wärtsilä Finland Oy. The authors acknowledge the Knut and Alice Wallenberg Foundation, the Swedish Energy Agency, Vinnova and the Swedish Research Council for financial support, as well as the European Network for Electron Microscopy (ESTEEM2, European Union Seventh Framework Programme under Grant Agreement 312483-ESTEEM2 (Integrated Infrastructure Initiative-I3)).

Conflict of interest

The authors declare no conflict of interest.

Keywords: electron microscopy · oxidation · palladium · platinum · scanning probe microscopy

- [1] a) R. M. Heck, R. J. Farrauto, S. T. Gulati, *Catalytic Air Pollution Control*, Wiley, Hoboken, **2009**; b) C. D. Falk, J. J. Mooney, SAE International, **1980**; c) S. Roy, A. Baiker, *Chem. Rev.* **2009**, *109*, 4054–4091; d) G. Liu, P.-X. Gao, *Catal. Sci. Technol.* **2011**, *1*, 552; e) N. Takahashi, H. Shinjoh, T. Iijima, T. Suzuki, K. Yamazaki, K. Yokota, H. Suzuki, N. Miyoshi, S.-i. Matsumoto, T. Tanizawa, T. Tanaka, S.-s. Tateishi, K. Kasahara, *Catal. Today* **1996**, *27*, 63–69; f) A. Russell, W. S. Epling, *Catal. Rev.* **2011**, *53*, 337–423.
- [2] a) J. Yang, V. Tschamber, D. Habermacher, F. Garin, P. Gilot, *Appl. Catal. B* **2008**, *83*, 229–239; b) F. J. Gracia, L. Bollmann, E. E. Wolf, J. T. Miller, A. J. Kropf, *J. Catal.* **2003**, *220*, 382–391; c) X. Chen, J. Chen, Y. Zhao, M. Chen, H. Wan, *Chin. J. Catal.* **2012**, *33*, 1901–1905; d) M. Ozawa, T. Okouchi, M. Haneda, *Catal. Today* **2015**, *242*, 329–337; e) G. S. Zafiris, R. J. Gorte, *J. Catal.* **1993**, *140*, 418–423.
- [3] a) M. R. Ward, T. Hyde, E. D. Boyes, P. L. Gai, *ChemCatChem* **2012**, *4*, 1622–1631; b) A. T. DeLaRiva, T. W. Hansen, S. R. Challa, A. K. Datye, *J. Catal.* **2013**, *308*, 291–305; c) X. Chen, Y. Cheng, C. Y. Seo, J. W. Schwank, R. W. McCabe, *Appl. Catal. B* **2015**, *163*, 499–509; d) R. J. Liu, P. A. Crozier, C. M. Smith, D. A. Hucul, J. Blackson, G. Salaita, *Microsc. Microanal.* **2004**, *10*, 77–85.

- [4] a) T. R. Johns, J. R. Gaudet, E. J. Peterson, J. T. Miller, E. A. Stach, C. H. Kim, M. P. Balogh, A. K. Datye, *ChemCatChem* **2013**, *5*, 2636–2645; b) A. Morlang, U. Neuhausen, K. V. Klementiev, F. W. Schütze, G. Miehe, H. Fuess, E. S. Lox, *Appl. Catal. B* **2005**, *60*, 191–199; c) G. W. Graham, H. W. Jen, O. Ezekoye, R. J. Kudla, W. Chun, X. Q. Pan, R. W. McCabe, *Catal. Lett.* **2007**, *116*, 1–8; d) O. K. Ezekoye, A. R. Drews, H. W. Jen, R. J. Kudla, R. W. McCabe, M. Sharma, J. Y. Howe, L. F. Allard, G. W. Graham, X. Q. Pan, *J. Catal.* **2011**, *280*, 125–136; e) K. Kallinen, A. Moreno, A. Savimäki, T. J. J. Kinnunen, SAE Technical Paper 2009-26-0018, **2009**; f) C. Carrillo, T. R. Johns, H. Xiong, A. DeLaRiva, S. R. Challa, R. S. Goeke, K. Artyushkova, W. Li, C. H. Kim, A. K. Datye, *J. Phys. Chem. Lett.* **2014**, *5*, 2089–2093; g) H. Xiong, E. Peterson, G. Qi, A. K. Datye, *Catal. Today* **2016**, *272*, 80–86; h) T. R. Johns, R. S. Goeke, V. Ashbacher, P. C. Thüne, J. W. Niemantsverdriet, B. Kiefer, C. H. Kim, M. P. Balogh, A. K. Datye, *J. Catal.* **2015**, *328*, 151–164.
- [5] a) R. Leary, Z. Saghi, M. Armbrüster, G. Wowsnick, R. Schlögl, J. M. Thomas, P. A. Midgley, *J. Phys. Chem. C* **2012**, *116*, 13343–13352; b) S. Bals, B. Goris, L. M. Liz-Marzán, G. Van Tendeloo, *Angew. Chem. Int. Ed.* **2014**, *53*, 10600–10610; *Angew. Chem.* **2014**, *126*, 10774–10784; c) J. Zečević, K. P. de Jong, P. E. de Jongh, *Curr. Opin. Solid State Mater. Sci.* **2013**, *17*, 115–125; d) J. Zečević, A. M. J. van der Eerden, H. Friedrich, P. E. de Jongh, K. P. de Jong, *ACS Nano* **2013**, *7*, 3698–3705.
- [6] a) S. Van Aert, A. De Backer, G. T. Martinez, B. Goris, S. Bals, G. Van Tendeloo, A. Rosenauer, *Phys. Rev. B* **2013**, *87*, 064107; b) A. B. Yankovich, B. Berkels, W. Dahmen, P. Binev, S. I. Sanchez, S. A. Bradley, A. Li, I. Szlufarska, P. M. Voyles, *Nat. Commun.* **2014**, *5*, 4155.
- [7] T. Pingel, M. Skoglundh, H. Grönbeck, E. Olsson, *J. Microsc.* **2015**, *260*, 125–132.
- [8] J. W. Geus in *Catalyst Preparation* (Ed.: J. Regalbuto), CRC, Boca Raton, **2006**, pp. 341–372.
- [9] a) P. L. Gai, L. Lari, M. R. Ward, E. D. Boyes, *Chem. Phys. Lett.* **2014**, *592*, 355–359; b) X.-F. Yang, A. Wang, B. Qiao, J. Li, J. Liu, T. Zhang, *Acc. Chem. Res.* **2013**, *46*, 1740–1748.
- [10] E. Wicke, *Chem. Ing. Tech.* **1957**, *29*, 305–311.
- [11] P. B. Weisz, C. D. Prater in *Advances in Catalysis, Vol. 6* (Eds.: V. I. K. W. G. Frankenburg, E. K. Rideal), Academic Press, New York, **1954**, pp. 143–196.
- [12] D. M. Nicholas, Y. T. Shah, *Ind. Eng. Chem. Prod. Res. Dev.* **1976**, *15*, 35–40.
- [13] E. C. Akubuiro, X. E. Verykios, L. Lesnick, *Appl. Catal.* **1985**, *14*, 215–227.
- [14] R. H. Nibbelke, M. A. J. Campman, J. H. B. J. Hoebink, G. B. Marin, *J. Catal.* **1997**, *171*, 358–373.
- [15] a) Y. F. Chu, E. Ruckenstein, *J. Catal.* **1978**, *55*, 281–298; b) S. B. Simonsen, I. Chorkendorff, S. Dahl, M. Skoglundh, J. Sehested, S. Helveg, *J. Am. Chem. Soc.* **2010**, *132*, 7968–7975; c) S. B. Simonsen, I. Chorkendorff, S. Dahl, M. Skoglundh, J. Sehested, S. Helveg, *J. Catal.* **2011**, *281*, 147–155; d) P. Loof, B. Stenbom, H. Norden, B. Kasemo, *J. Catal.* **1993**, *144*, 60–76.
- [16] W. S. Rasband, in U.S. National Institutes of Health, Bethesda, Maryland, USA, <http://imagej.nih.gov/ij/>, **1997–2015**.
- [17] S. Brunauer, P. H. Emmett, E. Teller, *J. Am. Chem. Soc.* **1938**, *60*, 309–319.
- [18] M. Dudák, V. Novák, P. Kočí, M. Marek, P. Blanco-García, G. Jones, *Appl. Catal. B* **2014**, *150*, 446–458.

 Manuscript received: March 17, 2017

Accepted manuscript online: March 23, 2017

Version of record online: June 20, 2017